JOM, Vol. 75, No. 10, 2023
https://doi.org/10.1007/s11837-023-06045-5

Microstructure and Elevated Temperature Flexure Testing of Tungsten Produced by Electron Beam Additive Manufacturing

HAOZHI ZHANG,[1] PAUL R. CARRIERE,[3] EMMANUEL D. AMOAKO,[1] CHRIS D. ROCK,[2] SEIJI U. THIELK,[3] COLIN G. FLETCHER,[1] and TIMOTHY J. HORN [1,4]

1.—Mechanical and Aerospace Engineering Department, North Carolina State University, 915 Partners Way, Raleigh, NC 27607, USA. 2.—Center for Additive Manufacturing and Logistics, North Carolina State University, Raleigh, NC 27607, USA. 3.—RadiaBeam Technologies, LLC, Santa Monica, CA 90404, USA. 4.—e-mail: tjhorn@ncsu.edu

Due to their superior high-temperature thermomechanical capabilities, sputter erosion durability, and excellent resistance to hydrogen isotopes, tungsten materials have garnered significant interest in fusion nuclear applications. However, low room-temperature ductility and complex machining strategies present significant challenges for traditional fabrication. Electron beam powder bed fusion (EB-PBF) shows promise in manufacturing pure tungsten via high thermal energy input, elevated build temperature, and a tightly controlled high-vacuum environment. This work explores the process, structure, and property relationship of pure tungsten fabricated by EB-PBF, where 99.8% relative density was achieved with reduced cracking by isolating the build substrate and optimizing the print parameter suite. Optical and electron imaging revealed that the microstructure contained equiaxed grains along the build direction, with subgrains present in all inspected grains. Flexural testing at ambient and elevated temperatures demonstrated high ductility at 900°C and flexural strength of 470 MPa at room temperature of additively manufactured tungsten.

INTRODUCTION

Tungsten exhibits desirable properties for nuclear fusion applications, including its low coefficient of thermal expansion (4.5×10^{-6} K^{-1}), low sputtering yield, high melting point (~3422°C), high thermal conductivity (~108 W/mK in operation), and resistance to hydrogen isotopes.[1–4] However, tungsten's high hardness and low ductility at room temperature present significant challenges for traditional forming, milling, and joining processes.[5] This has motivated extensive research in recent years to explore alternative methods like spark plasma sintering[6,7] and additive manufacturing (AM) as a potential substitute approach. The precise and complex geometries required for fusion reactor components may be more easily achieved using AM techniques, which allow for the layer-by-layer buildup of the material without the need for complex machining or assembly. Additionally, the layer-wise building nature of additive manufacturing provides the opportunity for in situ process monitoring, which can be used to detect defect formation in real time and to inform future builds.[8] Consequently, AM has emerged as a promising solution for fabricating tungsten-based components.[9–11]

To date, laser powder-bed fusion (LPBF) of tungsten has received significant attention. However, achieving dense tungsten material using this method has proven challenging due to several factors, including its high melting temperature, high thermal conductivity, and low absorption at the typical ~ 1 μm wavelength utilized in commercial AM systems. These factors can result in

(Received May 15, 2023; accepted July 24, 2023; published online August 30, 2023)

incomplete melting and solidification, causing defects such as porosity and incomplete fusion in the final product.[12–22] Moreover, LPBF of W has also been associated with a propensity for cracking attributed to various causes.[23] Several approaches have aimed to mitigate cracking during LPBF, such as the spheroidization of powder feedstocks,[14] increasing the substrate temperature above the ductile to brittle transition temperature (DBTT),[20,24] hot isostatic pressing,[15,25] atmosphere control,[26] variations in scan strategy,[20,27] and laser surface remelting.[28] Intergranular fracture is the most common cause of failure in AM of W and is partially attributable to the high ductile to brittle transition temperature, which is dependent on oxygen concentration and ranges from $\sim$ 200°C to 600°C.[29] The low ductility is related to a lack of close-packed planes in its BCC structure, low dislocation density, the difficulty of the dislocation slip motion, and poor grain boundary cohesion, which is exacerbated by the segregation of interstitial contamination (e.g., O, C, H, N, K, P) during solidification.[30–32] Also, Wang et al. reported that oxygen contamination tended to complicate LPBF AM processing and has two primary sources: the high specific surface area of the intrinsically oxidized powder and the LPBF processing chamber atmosphere.[33] Increased the oxygen content was found to modify the surface tension and viscosity of the melt pool, which tended to favor balling over wetting during melting, further contributing to the poor quality of LPBF tungsten.[34] However, cracks were reduced but not eliminated, even when the oxygen level was tightly controlled during the LPBF process,[35] suggesting that contamination may not be the only factor affecting the crack formation.

Vrancken et al. used LPBF single-track melting experiments in tungsten to identify that the beam power and cracking distance have an inverse relationship.[36] While it is intuitive that high power is required to achieve a stable melt pool and thus high density, the keyhole phenomenon may even worsen the porosity with the increased energy inputs.[21] Crack frequency and pattern were related not only to the energy density but also to the scan strategy used.[20] The right combination of printing parameters helps to produce a denser tungsten part, but it is still challenging to eliminate cracks by only adjusting processing parameters.[27] Several studies on increasing the substrate temperature of LPBF above DBTT have also been conducted.[24,35,37] High ambient temperatures during LPBF factor into improvements in density, but they cannot address the root cause to mitigate cracks alone.

While the reporting in the literature is sparse, electron beam powder bed fusion (EB-PBF) has shown promise in manufacturing tungsten. The efficiency of the EB-PBF process is typically high where the kinetic energy of the accelerated electrons is transferred to the material and the interaction volume is in the order of a few microns. The fast deflection capabilities of the beam facilitates high processing and preheating speed of the powder bed by repeatedly scanning a defocused beam at high power and high velocity to raise the temperature to $\sim$ 1200–1800°C prior to the melting procedure.[38,39] Additionally, the vacuum environment is attractive for tungsten to minimize the inherent oxidation risk.[40,41] The vacuum processing environment also eliminates convective heat losses, which can be significant due to the high velocity shielding gas associated with L-PBF.[42]

Yang et al. investigated the processing parameters for tungsten using EB-PBF, achieving an optically measured relative density of 99.5% for 10 $\times$ 10 mm samples. In Yang's study, the substrate temperature was raised to 800–950°C, and the resulting samples exhibited columnar crystal structure, as well as intergranular cracking.[43] Wright studied the correlation of porosity with the processing parameter of EB-PBF, achieving reduced cracks and high density tungsten samples at the elevated preheating temperature of 1000°C.[44] Dorow-Gerspach et al. also reported a similarly dense tungsten material, processed at an environment temperature of 1000°C, resulting in a columnar grain structure. While micro-cracking was observed, these samples were subjected to static (10 MW/m^2) and transient (105 pulses with 0.14 GW/m^2) heat loads and showed comparable performance with respect to conventionally processed and recrystallized tungsten.[45] A relative density of > 98% was achieved by Ren et al. using non-spherical powder with an ambient temperature of 1150°C.[46] In a precursor to the present study, crack density was significantly lowered, and micro-crack-free regions were observed when the preheating temperature was elevated to 1500°C, according to Ellis et al.[38] The processing windows of EB-PBF to produce highly dense, crack-free tungsten material was further developed by Ledford et al. increasing the ambient surface temperature to 1800°C, and observing a pronounced (001) to (111) change in texture with decreasing beam speed and current within the dense processing space.[39]

While most EB-PBF-related studies concentrate on the high power density and elevated surface temperature to produce the tungsten for fusion energy application, a complementary method was adopted in this work. A vacuum isolation layer underneath the build substrate, which limits the heat conduction through the substrate, is introduced to stabilize the extremely high surface temperature. A prismatic tungsten geometry was manufactured using this setup and the parameters adopted from a prior effort.[38] Samples harvested from the geometry were extracted and four point flexural tests were conducted to compare the as-fabricated AM samples and wrought tungsten at room temperature and at an elevated temperature of 900°C in the ambient atmosphere environment.

EXPERIMENTAL

Powder Characteristics

Tungsten powder, produced by chemical synthesis and then plasma spheroidized, was procured from Tekna Advanced Materials (Quebec, Canada). The powder particle size distribution was quantitatively analyzed using a Microtrac S3500 laser diffraction particle analyzer following a wet method protocol with ultrasonic agitation. The oxygen content of the original tungsten powder was measured by inert gas fusion using LECO OH 836, referencing the refractory alloy protocol (Method No. 203-821-427). The bulk elemental composition was determined by glow discharge mass spectroscopy (GDMS), via Eurofins EAG Laboratories, with no indication of trace contaminants above the background. The raw powder material was stored in a sealed, inert environment before each use.

Sample Fabrication

All the samples were manufactured using a modified Arcam S12 electron beam melting system. A controlled chamber vacuum level of 10^{-3} mbar was maintained through a controlled bleed of Grade-VI purity helium into the chamber during printing.[41,47] A 40-mm-diameter by 5-mm-thick pure tungsten sputtering target lid (Changsha Advanced Engineering Materials) was utilized as the build substrate. To reduce conductive heat transfer through the build plate, it was placed on a tungsten crucible to purposely create a vacuum isolation layer. The cup was then placed in a 1-mm-deep pocket machined molybdenum plate. This assembly, illustrated in Fig. 1, was placed within the AM build piston and surrounded with tungsten powder, level with the top surface of the tungsten sputtering target lid. The build substrate temperature and the subsequent powder bed surface temperature were continually monitored with a two-color high-temperature pyrometer (Fluke Endurance E1R1) through a viewport. A target surface temperature of 1800°C was selected for all the printing processes in the present study, and maintained at the temperature for a minimum of 1 h prior to spreading the first powder layer.

The preheat and melt parameters were adopted from Ti-6Al-4 V standard settings with the software version 3.0.27 on the Arcam S12 machine, where the preheat was used prior to each layer melting to maintain 1800°C for the duration of the build. In addition, the melting processing window was investigated by a prismatic trial printing, in which the volumetric energy density was intentionally varied from the bottom to the top until the full dense layer was observed. The final melting parameters are listed in Table I, where the relatively low beam current, slow melt speed, and tight hatch spacing were used to melt each layer to avoid significant process defects and porosity.

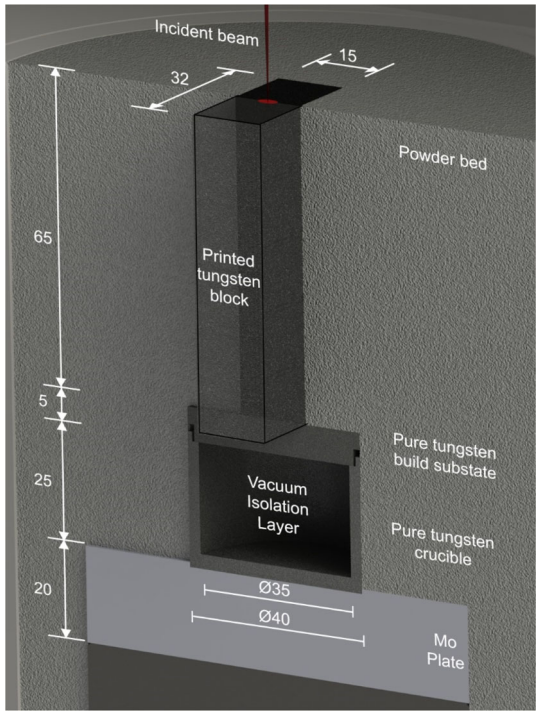

Fig. 1. Schematic of the build chamber and vacuum isolation setup which maintaining the high bed surface temperature during the electron beam powder bed fusion (EB-PBF) print process.

It is important to note that the control system of the Arcam EB-PBF system constantly changes the beam speed and the beam current, based on an open loop feedforward control strategy optimized for Ti-6Al-4 V to maintain a constant surface temperature and melt pool size. While the parameters listed above are necessary for the repeatability of the study, they are not necessarily the speed and current that the control system used for melting. Therefore, the beam speed was directly tracked by monitoring the beam position using the deflection coil feedback voltage. Beam speeds were then calculated from these positions, and the incident beam current was recorded by measuring the high-voltage command feedback signal. Additionally, an in situ backscatter detector was used to collect in-process images, which can be used to ascertain part density. All the data were recorded at 500 kHz following the methodology of Ledford et al.[48] For the precise replication of this experiment, please see Table SI for the input parameter values of the Arcam S12 machine (refer to online supplementary material). The rectangular block measuring 15 mm width × 32 mm length × 65 mm high was produced using these input parameters, as shown i in Table I.

Sample Characterization

Upon completion of the AM process and cooling under vacuum, the rectangular block part was retrieved from the chamber, and powder was manually removed. The metallurgical and flexure

Table I. Key EB-PBF melt and preheat parameters used to fabricate the flexural testing samples

Preheat parameters		Melt parameters	
Min beam current (mA)	20	Beam current (mA)	10
Max beam current (mA)	48	Beam speed (mm/s)	300
Beam speed (mm/s)	14,600	Focus offset (mA)	10
		Layer thickness (μm)	70
		Hatch spacing (μm)	30

The values are developed from standard Ti-6Al-4V settings on the Arcam S12 machine based on software version 3.0.27.

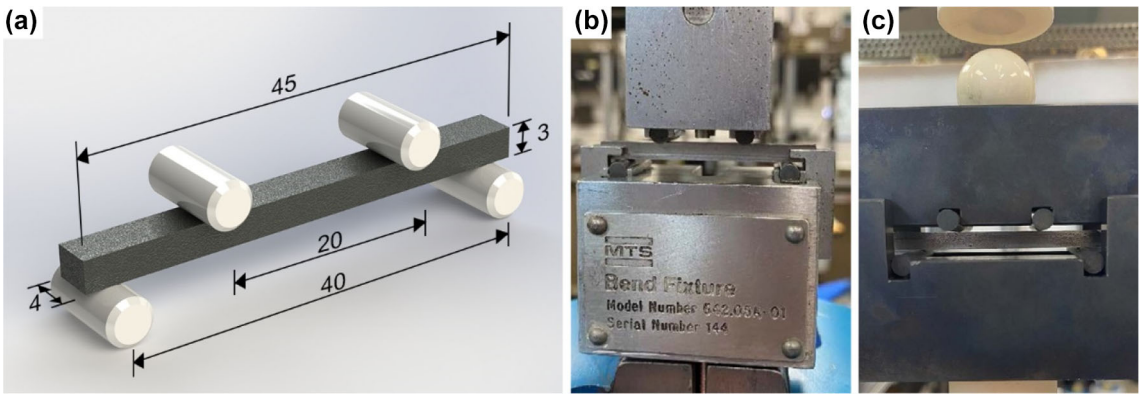

Fig. 2. (a) Schematic of specimen dimensions (in millimeter) relative to the fixture spans, with the image of the mechanically prepared tungsten specimen loaded into the fixtures: (b) based on ASTM C1161-18 configuration B, and (c) based on ASTM C1211-02 configuration B.

testing specimens were then extracted from the block by wire electric discharge machining (EDM). Flexure testing specimens measuring 45 × 4 × 3 mm geometry were harvested from the printed samples in accordance with ASTM C1211-02 size B specification, as shown in Fig. 2. As a comparison, the hot-rolled tungsten plates procured from Ed Fagan were harvested by EDM. All the samples were then manually ground on each face with 600-grit SiC paper to remove the recast layer. The density of the specimens was measured by a gas pycnometer. Metallurgical samples were prepared by sectioning, mounting, and grinding with a polish using 0.05 μm diamond solution and vibratory polished with 0.02 μm colloidal silica as the last step. The necessary etching was conducted after final polishing for 30 s with the etchant comprised of 25% HF, 25% HNO_3, 25% H_2O_2, and 25% deionized water. Microstructure analysis of the testing samples was carried out using JEOL 6010LA scanning electron microscope (SEM) and Keyence KX optical microscope. The electron backscatter diffraction (EBSD) data were imaged on an FEI Helios Hydra CX dual beam scanning electron microscope.

Flexural Testing

The four-point flexural bending approach was chosen due to the expected brittle failure mode at room temperature and the induced tensile failure. The flexural testing was conducted externally by Touchstone Testing Laboratory. Both wrought and AM tungsten flexure samples were tested at room temperature (25°C) per ASTM C1161-18 and at elevated temperature (900°C) per ASTM C1211-02 on an MTS 810 load frame at a loading rate of 0.50 mm/min. The room-temperature specimens were tested with a fully articulating bend fixture (642.05A-01), and the high-temperature specimens were tested with a fully articulating silicon carbide fixture. Both tests had a 20 mm upper span and a 40 mm lower span, as depicted in Fig. 2. The high-temperature samples were heated at a rate of 48.9°C/min with a 5 min soak time.

RESULTS

Powder Characteristics

Figure 3 shows the backscatter electron microscopy of the as-received plasma-spheroidized tungsten powder. The 10th, 50th, and 90th percentiles of the powder was measured at 57 μm, 72 μm, and 98 μm, respectively. The powder shows a generally

spherical morphology with several particles that appear to have hollow regions. The oxygen content of the fresh powder was measured as 210.6 ± 4.2 ppm (calculated from three consecutive measurements). Table II shows the trace elemental analysis by glow discharge mass spectroscopy where the total solute impurities are less than 50 ppm total. The elements chosen in Table II are based on refractory elements first, then by the elements' weight percentage over 0.1 ppm with all other trace elements omitted.

As-fabricated Sample Characteristics and Microstructure

The density of the printed specimens was measured by a gas pycnometer at 19.23 ± 0.02 g/cm^3, which closely matches the nominal tungsten density of 19.25 g/cm^3, suggesting that the processing parameters selected and incorporation of isolating layer can produce an almost full dense tungsten part with the relative density of 99.8%.

Optical micrographs of the *X–Z* and *X–Y* planes of the sample after room-temperature flexural testing and metallurgical etching are shown in Fig. 4, and reveal the surface topology differences after etching, with no clear crystallography texture, such as columnar grains, reflected along the build direction throughout the specimen. Sporadic cracks and pores can be seen in the enlarged area images, where the crack density was negligible compared to the surface area of the specimens. The confocal micrograph of unetched cross-sections from different specimens can be seen in Figure S1 (refer to online supplementary material).

Figure 5a shows SEM backscatter images which also reveal an equiaxed microstructure in the AM tungsten material, with the grain size in the range of 10–100 μm. The enlarged area containing 10 to 20 μm subgrains is depicted in the higher-magnification image in Fig. 5b. This fine grain structure is much smaller than the etched grains from Fig. 4, which are in the range of 100–200 μm. The subgrain crystallographic orientations were revealed by backscatter electron contrast and light etching from the colloidal silica final polishing.

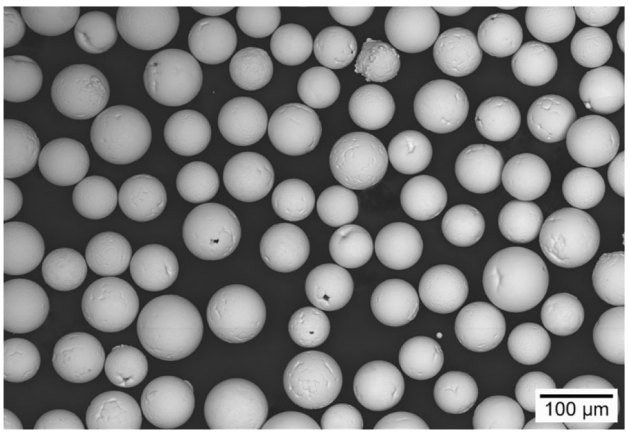

Fig. 3. Backscatter electron microscopy of the as-received plasma-spheroidized tungsten powder depicting spherical morphology.

Figure 6a shows the EBSD map of the microstructure along the build direction (*Y–Z* plane), the data presenting a mixed crystallographic texture in the (111) and (101) orientations, which is commonly reported in EB-PBF tungsten material,[22,23] while Fig. 6c shows a dominant texture near the (111) direction on the *X–Y* plane of the same sample. Interestingly, the EBSD of the *Y–Z* plane shows a mix of columnar and equiaxed grains, which is different from the pure equiaxial microstructure observed in Fig. 5. The EBSD data further indicate that the ~ 10-μm size grains in Fig. 5 could be subgrain structures within the larger grains, a pattern which differs from recent reports on EB-PBF tungsten.[38,39,43–46] The preferential (111) grain orientation matched the result obtained from Ellis' study, which, however, showed epitaxial grains.[38] The microstructure difference between this study and others might be the convoluted effect of low cooling rate-induced columnar-to-equiaxed transition and dynamic recrystallization due to the thermal stress.

Figure 6b and d exhibit the grain boundary misorientation distribution map on the *Y–Z* and *X–Y* planes, respectively. The measured fraction of the low-angle grain boundary (1–15°) on both the *Y–Z* and *X–Y* planes is over 95%, as presented by the misorientation angle data chart in the figure. The extremely high percentage of the low-angle grain boundary further confirmed the ubiquitous appearance of subgrains on both the build and transverse directions. The high angle grain boundary on the *Y–Z* plane demonstrates the appearance of a bimodal distribution of columnar and equiaxed grain structure, and only equiaxed grains can be seen on the *X–Y* plane. The correlation between the density of high-angle grain boundaries and cracks in the AM tungsten material was commonly observed in other studies.[14,22,49,50] Furthermore, cracking was found to have a higher tendency to form along the high-angle grain boundaries, where the fracture helps to relieve intergranular stresses.[17]

Cracks in the as-fabricated solids were also explored by examining the microcracking at a grain boundary triple point. Figure 7a shows the EBSD image quality of the intersection point of three large equiaxed grains, where the intergranular cracks are visible along all three grain boundaries, and features suggest the presence of stresses during the AM process. Voids are present along the boundaries, possibly due to gas pore formation during melting and are further pushed to the grain boundary during the cooling process. The dark spots inside the grains, and the accompanying streaks, are residual contaminants on the sample surface. The appearance of pores seems to facilitate the initiation and propagation of the cracks, as some were found initiating from the pores. The pore formation and

Table II. The glow discharge mass spectroscopy (GDMS) result of *W* powder (ppm in wt.%), the selection sequence is refractory elements first, followed by other elements > 0.1 ppm, while the oxygen content was measured by inert gas fusion using LECO OH 836, referencing the refractory alloy protocol

W	Ta	Mo	Hf	Nb	Fe	Cr	Ni	Zn	Oxygen
Bal	< 5	2.7	0.04	0.06	12	1.1	0.47	0.18	210

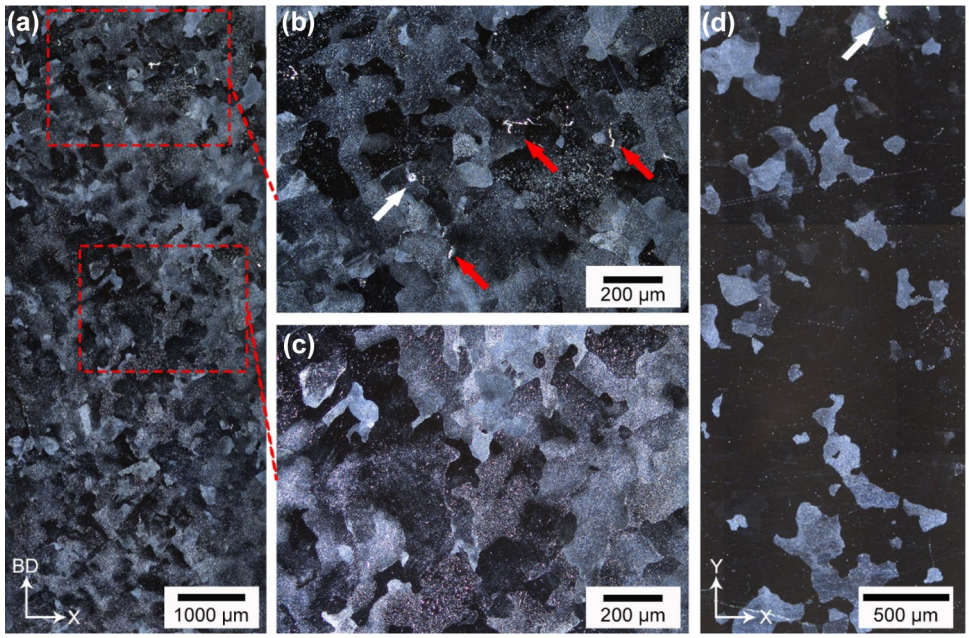

Fig. 4. Large area optical micrograph in (a) *X*-build direction plane with (b) enlarged area with defects and (c) enlarged area without defects; (d) optical micrograph in the *X*–*Y* plane of the etched flexural sample showing equiaxed microstructure. White arrows indicate the internal porosities, and red arrows highlight microcracks.

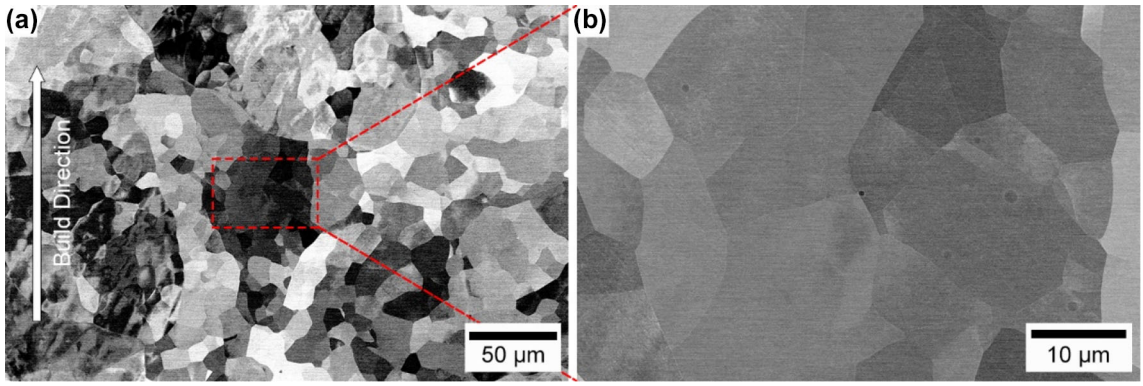

Fig. 5. Representative backscatter image of microstructure under (a) × 500 and (b) × 3500 showing the equiaxial grain structure, cell-like subgrains, and no obvious cracks along the build direction in the field of view.

cracking behavior in this work are consistent with the observation of Wang et al.[33] A distinct subgrain structure, with cells on the order of 10 μm in size, is visible in all grains, and an inverse pole figure of the same region (Fig. 7b) enhances the visibility of the subgrain structure and reveals localized misorientation in the immediate vicinity of cracks. The kernel average misorientation of this region (Fig. 7c) shows local misorientation along the cracks as well as the subgrain boundaries. To further enhance the visibility of misorientations along grain boundary cracks, in-grain misorientations have been shaded relative to an arbitrary point near the center of each grain (Fig. 7d). The resulting image depicts orientations that differ from the grain center, with bright colors (e.g., orange, yellow, white), while regions

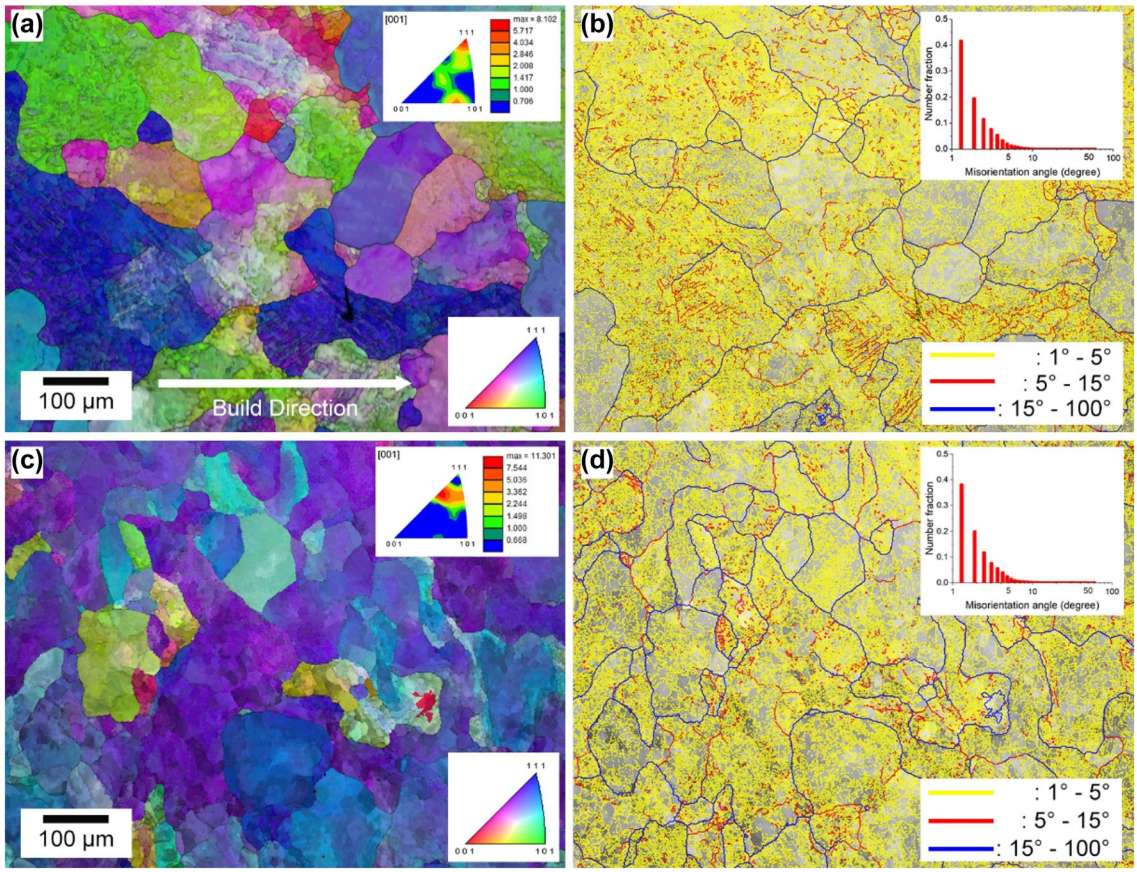

Fig. 6. (a) Electron backscatter diffraction (EBSD) micrograph with grain orientation intensity map and, inset, the inverse pole figure coloration reference, and (b) the grain boundary misorientation distribution map with, inset, the number fraction data of the *Y–Z* cross-section from the as-printed tungsten sample. (c) EBSD micrograph with grain orientation intensity map, and (d) grain boundary misorientation distribution map of the *X–Y* cross-section from the same tungsten sample. The equiaxed microstructure with fine subgrains is obvious in both investigated *X–Y* and *Y–Z* planes.

with similar orientations are darker shades of red or black. The bright region, obvious within approximately 10 μm thickness adjacent to the crack, is possibly due to the released thermal stress along the grain boundaries.[24] This relative misorientation color coding method further highlights the strain concentration within the grain and next to the cracks from the subgrain orientation perspective. Such intergranular cracks were found to have a very low density in our printed tungsten material because over 99% of the area fraction of the cross-section was crack-free, based on the image analysis.

Flexural Testing of EB-PBF Fabricated Tungsten

A schematic of the flexural testing sample preparation and experiment setup is shown in Fig. 2. Prepared AM tungsten and wrought tungsten specimens were tested atmospherically at room temperature and an elevated temperature of 900°C. The comparison result of the stress–displacement curve can be seen in Fig. 8a, and the relative optical images of the tested samples are shown in Fig. 8b.

The stress–displacement curves in Fig. 8 demonstrate the expected brittle behavior for AM and wrought specimens at room temperature with a linear increase in stress and subsequent failure at the onset of plastic deformation. The AM tungsten specimen cracked within the inner gauge section and was completely fractured into two unequal pieces. In contrast, the four-point bend testing was immediately stopped when the crack was observed on the wrought sample's reverse side of the loading contact point. This explains the apparently higher flexural strength of the tungsten AM compared to the wrought counterpart at room temperature. The crack propagation on the wrought tungsten specimen shows that it is not a break-through fracture.

Ductile behavior was observed for both specimen types at elevated temperatures, indicating that the 900°C test temperature exceeded the DBTT for both samples, as intended. At the same time, the AM specimen expressed a significantly lower yield and ultimate strength than the wrought part. Both specimens' elongation exceeded the range of the testing fixture without failure under the 0.5 mm/min loading rate. The flexural test of the AM sample

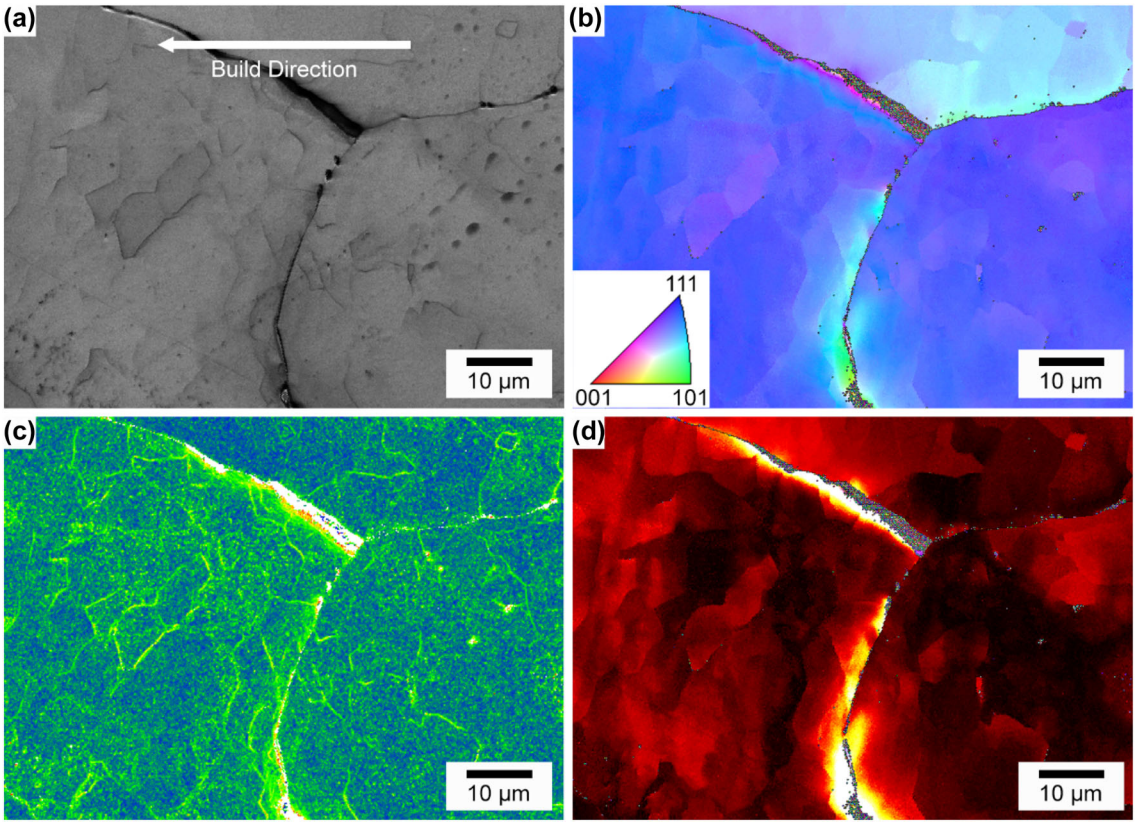

Fig. 7. (a) Image quality microscopy of the intergranular cracks and porosities observed along the grain boundaries in a grain intersection area, with (b) inverse pole figure map, (c) kernel average misorientation map, and (d) shaded grain angle map showing the subgrain distribution and misorientation within grains and adjacent to the cracks (color coding relative to an artificial orientation near the center of each grain).

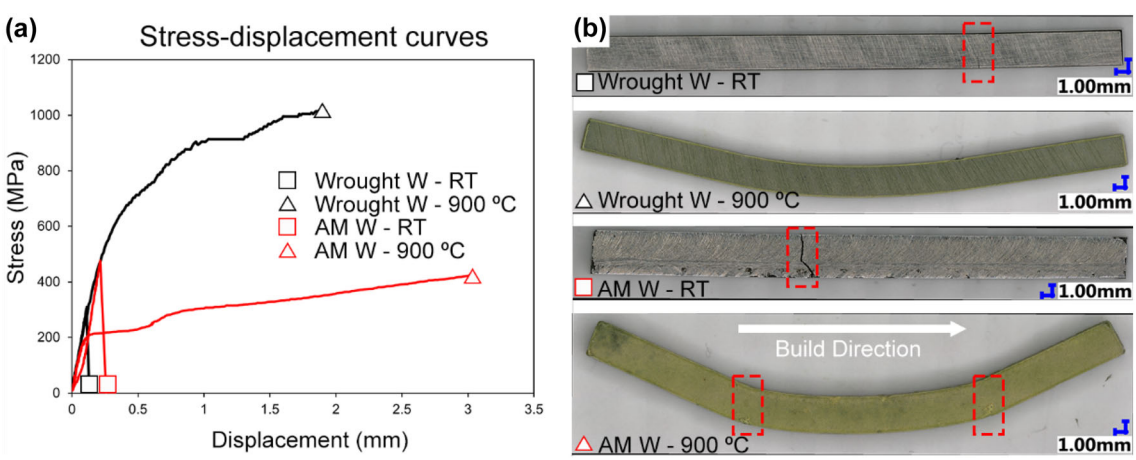

Fig. 8. (a) Stress–displacement curve of AM and wrought specimens tested at room temperature and 900°C, (b) the optical image after flexural testing with the highlighted (red-dashed square box) crack location on each sample.

at elevated temperatures shows a linearly increasing response after yield, which could result from roller sliding when the sample's elongation is beyond the testing fixture's limitation. The curvature observed on the AM sample is most likely due to the extended bending time, less rigid equiaxed microstructure, and the contact roller sliding compared to the texturized wrought counterpart. It is important to highlight that, while in this case the test was continued to observe the high ductility of both sample types, the four-point flexure test is only valid when deflections are small, so our analysis only considers these data and ignores the regions where deflections are high and complicated loading conditions exist.

The yellow color obtained on both the elevated temperature cases indicates that it is highly possible that the tungsten sample oxidized during the

flexural testing in ambient environments at 900°C. This coloration matched the observation of Habainy et al.[51] when pure tungsten was oxidized in different atmospheres at 906°C. The oxide formation on the surface and within the crack makes the crack less discernable compared to the room-temperature flexural samples. Some internal cracks and crack propagation from the surface can still be observed on the tension side of the AM tungsten bar tested at elevated temperature. However, no obvious external cracks were found on the wrought counterpart.

Figure 9a shows the side view of the fractured AM specimen under the four-point flexure test at room temperature in the ambient environment. The fracture origin can be observed on the tensile side, and the compression curl is on the opposite side where the compression is located. The pattern is a typical brittle fracture which can be classified as a medium-high energy failure mode based on ASTM C1161-18. Some porosity and porosity-induced cracks can be observed on the polished surface of the top compression side but are not apparent on the tension side. The defects observed in this region are more likely to be the lack of fusion due to the low beam energy other than gas pores formed along the grain boundary. Figure 9b shows the fracture surface of the broken bar presenting the tension crack region and compression curl region. The hackle lines and ridges help to locate the vicinity of a fracture origin, highlighted by the red dashed circle. Some coarse hackle lines (blue arrows) emanating from this volume-distributed flaw gradually pointed to the left side of the tension region, other than the circular radiating pattern, which could be due to the chain reaction of the crack and internal defects like porosities. While Fig. 9c further resolves the transition between the tension crack and the compression failure, a high-resolution secondary electron image of the crack origin location can be seen in Fig. 9d. The cleavage of the grains is more apparent on the tension side, and an obvious intergranular failure mode can be observed on the compression side, separated by the yellow dashed line. The size of the fracture origin and the underlying mechanism need to be further investigated to get an in-depth understanding of the failure mode of

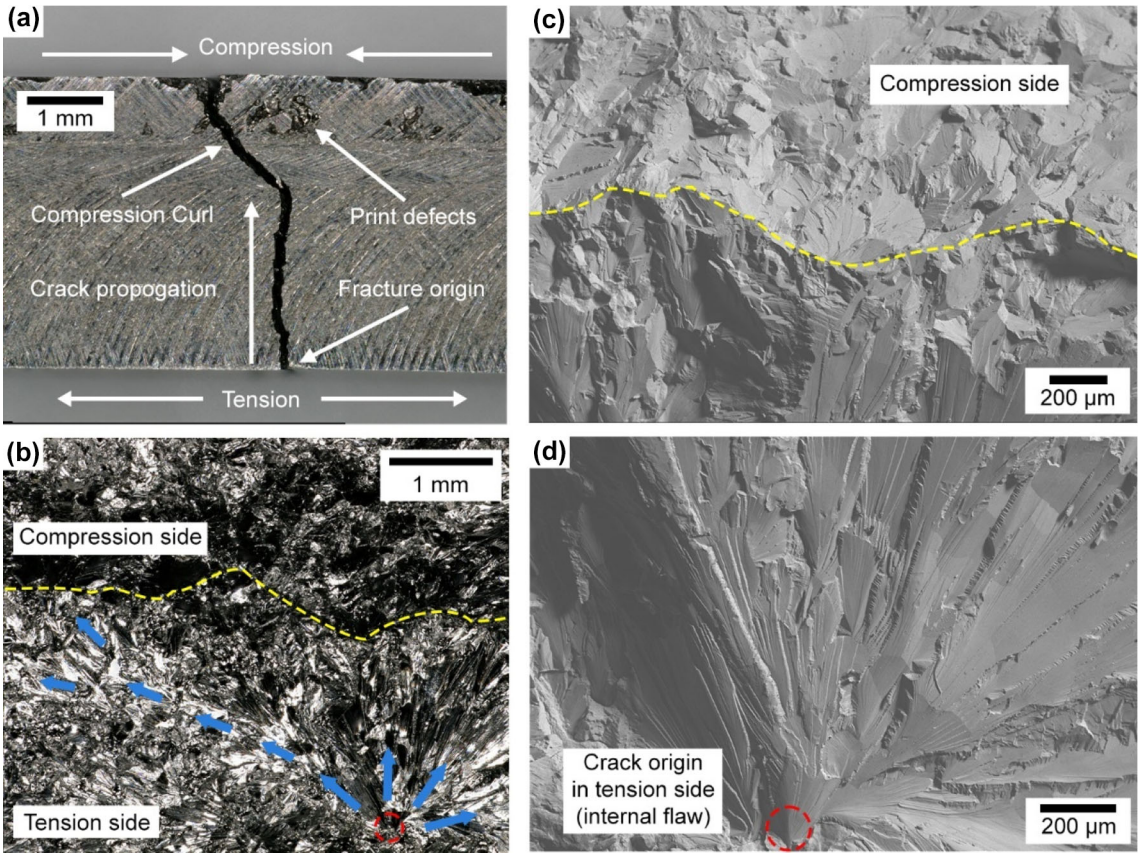

Fig. 9. (a) Schematic of the cracking from AM specimen four-point flexural testing at room temperature showing the fracture origin, propagation direction, and compression curl; (b) optical microscopy of the fracture surface, with (c) SEM of the transition area between the tension and compression failure, and (d) the internal defect-induced crack origin area. The red dashed circle represents the possible crack initiation location, the blue arrow aligns with the main hackle lines originating from the initiation point, and the yellow dashed line is the boundary between the tension and compression failure.

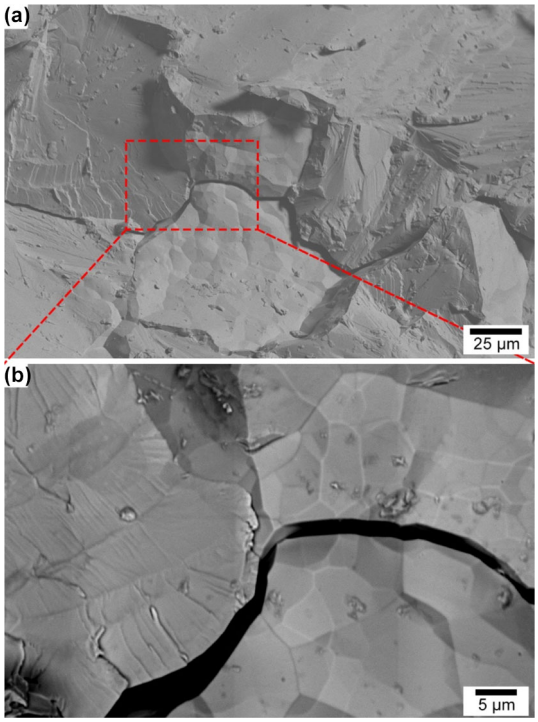

Fig. 10. (a) Backscattered electron micrograph showing the representative intergranular fracture inside the compression curl region of the failed flexural specimen, and (b) crack formed at a possible grain boundary triple point revealing cleavage fracture, inter-granular fracture, and the equiaxed subgrain structure.

AM tungsten. They could be attributed to the defects, like porosity and micro-cracks shown in Fig. 7, generated during the EBM melting process.

Figure 10a displays the typical intergranular fracture mode observed in the compression curl region of the flexural testing tungsten specimen produced by EBM. Equiaxed subgrain structures can be seen in the horizontal and vertical fracture planes. A higher-magnification backscattered electron micrograph in Fig. 10b depicts a possible grain boundary joint point in which the cleavage facet, intergranular crack, and subgrain microstructure are all clearly revealed. This crack pattern is similar to the misorientation analysis in Section "flexural testing of eb-pbf fabricated tungsten," suggesting that inherent defects, like inter-granular pores and micro-cracks, from the printing process are detrimental to the mechanical response of pure tungsten material. The stress concentration in the lack-of-fusion defects, gas entrapment pores, and micro-cracks under flexural testing conditions caused the crack initiation and quickly propagated through the sample. It is also suggested that the flexural testing result could be further improved by suppressing the appearance of those internal flaws via optimizing the print parameter suite.

DISCUSSION

Equiaxed Microstructure of As-fabricated Samples

The primary reason for the equiaxed microstructures and reduced cracking in the sample could be attributed to the combination of two factors: an elevated surface temperature of over 1800°C and the relatively small build area. These factors minimized intra- and inter-layer cooling as well as radiative cooling. Numerous studies[8,10,40,52] have indicated that the processing parameters are directly related to the spatial and temporal thermal signatures, affecting the part's solidification, solid-state transformation, residual stress evolution, and distortion behavior. The EB-PBF has the capability to control the local process parameters and deflection speed, enabling the researcher to efficiently heat the powder bed to extremely high temperatures, and to change the energy density to control the microstructure on a certain area in a given layer.[53]

In order to maintain the bed surface temperature stable at 1800°C, an isolation layer was introduced underneath the build substrate to mitigate the heat conduction loss during printing. The defocused electron beam repeatedly scans the powder bed at relatively high speeds and high beam currents. For the nominal EB-PBF process, like the AM of Ti-6Al-4 V, the preheat temperature typically ranges from 800°C to 1000°C due to the different build setups. In this research, however, the heating steps were distributed throughout and between the melting steps to maintain a constant heat flux through the powder bed surface. The beam heating of the entire powder bed was then repeated for each layer of the AM process to reach the constant surface temperature of 1800°C. This cyclic reheating maintains a stable high surface temperature, which may help to transform the columnar to equiaxed grain structure via decreasing the cooling rate of material underneath the interest area and reducing the thermal gradient along the build direction. For alloys, the columnar–equiaxial–transition (CET) typically occurs when the nucleation of numerous equiaxed dendrites takes place in the constitutionally undercooled liquid adjacent to the columnar dendritic front.[54–56] The columnar grains are generally coarse and characterized by anisotropic mechanical properties, while the equiaxed grains are usually small and with isotropic performance. Fine equiaxed grains can enhance the material properties, such as improving ductility and reducing solidification cracking.[57] Efforts have been made to quantitatively predict the CET for various alloys, where a low thermal gradient (G) and solidification rate (R) ratio favors the formation of equiaxed morphology instead of columnar grains in general.[58–60] The CET is occasionally reported in AM due to the thermal gradients in the AM process. In EB-PBF, grain orientation and texture modification have been

reported by tuning the thermal gradient and condition locally.[61–63] In our work, it is possible that constitutional supercooling does not fully explain the mix of equiaxed and columnar grains due to the 99.9% purity of tungsten. However, one complicating factor is the presence of 210 ppm oxygen content, making it unclear if a local variation of oxygen content would influence the supercooling condition which could partially result in CET. Frigola et al. observed the nearly equiaxed grain structure when a 99.8% low-purity powder or reused 99.9% high-purity powder was utilized for the EB-PBF of copper.[64] A similar near-equiaxed grain structure, which appears at a certain build height with relatively high beam power and beam speed, was reported by Guschlbauer et al. when producing high-purity 99.95% copper components.[65] Prithwish used the numerical model to predict the CET of a Cu-O system, and the equiaxed microstructure was reached by changing the process parameters and feedstock composition of the EB-PBF-processed pure copper.[66] However, none of those studies explained the formation mechanism of the equiaxed grain structure in terms of nucleation and grain growth under the influence of high oxygen content.

Besides the high bed temperature, the hatch spacing of 30 μm used in this work is relatively low compared with other studies, normally reporting a 300 μm hatch distance and about 250 μm full-width-half-maximum electron beam. Therefore, approximately nine out of ten area fractions of the previously deposited track were remelted during one scan pass. Ellis et al. determined that each point of the tungsten material was remelted approximately 14 times, compared with only 2 times for other existing studies, using a similar hatch spacing of 32.5 μm.[38] Remelting the previously deposited material more than once was found to positively mitigate crack formation but was still insufficient to suppress it entirely.[28] On the other hand, the effective local temperature before, during, and after melting is likely considerably higher than the target 1800°C with the appearance of a vacuum isolation layer. So, the cooling rate and temperature gradient in this work are likely lower than the traditional AM process which report CET and thermal stress relief under certain conditions.

The tight hatch spacing may also cause residual thermal stress accumulated from the repeated thermal cycle, and has been reported as the driving force for the recrystallization of AM components.[8] The plastic deformation imposed by repeated thermal stresses increases the dislocation density, where additional strains drive dislocations to form cell-like structures, and continued deformation results in the misorientation of the cell structures.[67] This mechanism is similar to dynamic recrystallization (DRX) during traditional hot working, and has been studied in the microstructure evolution of molybdenum during hot compression.[68] This mechanism is also observed in the electron beam welding process of tungsten,[69] and the electron beam floating zone melting treatment of single crystal tungsten.[70] A similar subgrain structure inside columnar molybdenum grains fabricated by EB-PBF was reported by Fernandez-Zelaia et al.,[71] and a lack of subgrain misorientation was observed possibly due to the early onset stage of DRX. Witzen et al.[72] also observed a similar cell-like dislocation pattern, which suggests that DRX occurred, in tantalum material manufactured by laser PBF. In a recent study of tungsten-fabricated EB-PBF, subgrain misorientation behavior was apparent,[39] including a pronounced "texture switch" from (001) to (111) with decreasing beam speed and current. Additionally, equiaxed low-angle subgrains within a columnar microstructure and a high dislocation density were also reported. The different orientations of cell-like subgrains observed along the build direction in this study are consistent with the presented result in our study and support DRX. Our high and maintained preheat temperature and "effective" cooling rate may exhibit a totally different grain morphology and size distribution compared to other AM tungsten reports.

The appearance of equiaxed parent grains and low-angle grain boundary cell-like subgrains are most likely the result of a combination of processes including the very high fabrication temperatures, the low cooling rate-induced CET, and strain-induced DRX with an onset of polygonization and grain growth. The resulting grain structure obtained in this work suggests that the suppressed cracking formation of the tungsten material, with an equiaxial grain structure along the build direction, can be produced under certain controlled circumstances.

Flexural Testing Analysis

It is crucial to acknowledge that Fig. 8 could potentially exhibit statistical scatter in the results due to the limited sample quantities used. Therefore, it would be premature to draw any definitive conclusions about the relative performance of the AM tungsten specimen and the wrought specimen. This is because flexural strength testing, being a non-deterministic quantity, is subject to variations between individual specimens. In order to qualitatively assess which material exhibits greater robustness under flexural testing, it would be necessary to conduct further experiments.

The testing standard used in this work was initially designed for the flexural testing of brittle materials, so it may not be a perfect candidate for testing ductile materials when elongation is over a particular range. On the other hand, to get a direct comparison between the flexural strength under

ambient and elevated temperatures, a consistent loading rate of 0.5 mm/min was used for all the tests. However, the testing rate should be chosen such that the time to failure was controlled within 10–30 s (ASTM C1211-18). Another standard of the four-point flexural test (ASTM D6272-17) also states that the test should be discontinued when the maximum strain in the tension side of the specimen reaches the threshold value and still no breaks occur. Nevertheless, this testing method is noteworthy due to its simplicity of high-temperature setup, less aggressive sample preparation, and clear differentiation between ductile and brittle response regimes. It represents a promising approach for investigating the thermal–mechanical behavior of AM tungsten and determining the DBTT. It is worth noting that there are few published reports on the tensile properties of AM tungsten, and those that do exist are not easily comparable due to differences in sample size, quantity, and experimental setup. A bending strength of 318 ± 52 MPa with less than 0.1 mm displacement was measured during the three-point bend testing of the 2 × 2 × 2.5 mm EB-PBF tungsten samples by Wright.[44] He reported that the poor mechanical behavior compared with rolled tungsten was attributed to large pores in the samples and residual stress imparted during the process. Another study using laser PBF-fabricated tungsten tensile testing bars exhibited almost no ductility and extremely low tensile strength (30–40 MPa) at test temperatures up to 500°C, due to the micro-cracks generated during fabrication and the high DBTT of tungsten.[73] Subscale and larger-scale miniature tensile testing were conducted by Ledford et al.[39] following the SSJ3 method, in the temperature range of 650–800°C, in both longitudinal and transverse orientations. The reported tensile property was closer to recrystallized tungsten wires, whereas the elongation was closer to wrought tungsten, but the result is highly anisotropic owing to the dominant columnar texture. For instance, the tensile strength of miniature samples fabricated from the transverse orientation and tested at 800°C were around 120 MPa with 0.12 mm maximum strain. On the other hand, the bending strength of the near-equiaxed grains fabricated in this study and tested at 900°C was approximately 200 MPa at a similar displacement and nearly no break-through happened after 0.3 mm displacement.

To some extent, the four-point flexural testing introduced in this work could be used as a baseline for a quantified and comparable mechanical test procedure for future reference to study the brittle and ductile behavior of tungsten materials. More steps between room temperature and 900°C, especially in the reported 300–600°C DBTT range, would be beneficial to test the DBTT behavior of AM tungsten but are not the focus of this work.

CONCLUSION

This investigation has explored the correlation between the fabrication process, microstructure, and properties of pure tungsten generated via electron beam powder bed fusion (EB-PBF). The parameter space was considered, and the build substrate was isolated, leading to a relative density of 99.8% with minimal cracking. Microstructural characterization was carried out using imaging and electron backscatter diffraction (EBSD), revealing the presence of equiaxed grains and subgrains in the build and transverse directions. Furthermore, flexural testing was performed at both ambient and elevated temperatures. The following conclusions can be drawn:

1. To maintain a constant bed temperature of 1800°C during the EB-PBF tungsten, an isolation vacuum layer was implemented. This resulted in the production of high-density (99.8%) pure tungsten parts, which were mostly free of cracks, with only a few isolated instances of cracking observed.
2. A mix of columnar and equiaxial grain structures close to the (111) and (001) orientations along with the build direction was observed in the as-fabricated part, which is distinctive from the dominant columnar textures from other AM-W publications.
3. Low-angle grain boundary cell-like subgrains were ubiquitous within the parent grains, no matter columnar or equiaxed shape, probably due to the columnar-to-equiaxed transition and dynamic recrystallization processes. The extremely high bed temperatures, possibly over 1800°C, and decreased cooling rate caused by substrate isolation and unique melting parameters like tight hatch spacing are the most likely contributing factors.
4. The printed tungsten block was sectioned into individual specimens for flexural bend testing at room temperature and the elevated temperature of 900°C, compared with the hot-rolled tungsten counterpart. The brittle behavior at room temperature and ductile behavior at 900°C were observed in both AM and wrought tungsten. The flexural strength of 470 MPa at room temperature was measured and the high ductility, more than 3 mm displacement, at 90°C was demonstrated by the EB-PBF tungsten. The linear response of the stress–displacement curve beyond a certain point in the elevated temperature testing case is possibly due to the testing system limitations, but still straightforward and easy enough to identify the DBTT of pure tungsten material.
5. This method is beneficial to investigate the brittle and ductile behavior of tungsten material with a standardized procedure, more straight-

forward sample preparation, and experiment setup compared with conventional tensile testing.

SUPPLEMENTARY INFORMATION

The online version contains supplementary material available at https://doi.org/10.1007/s11837-023-06045-5.

ACKNOWLEDGEMENTS

The experiment and analysis were performed at the Center for Additive Manufacturing And Logistics (CAMAL) of North Carolina State University under funding (no. # DE-SC0021700). This work was performed in part at the Analytical Instrumentation Facility (AIF) at North Carolina State University, which is supported by the State of North Carolina and the National Science Foundation (award no. ECCS-2025064). The AIF is a member of the North Carolina Research Triangle Nanotechnology Network (RTNN), a site in the National Nanotechnology Coordinated Infrastructure (NNCI).

AUTHOR CONTRIBUTION

HZ—Conceptualization, Investigation, Visualization, Writing—Original Draft. PRC—Funding acquisition, Conceptualization, Methodology, Writing—Original Draft, Writing—Review & Editing. EDA—Methodology, Investigation. CDR—Investigation, Visualization, Writing—Review & Editing. SUT Methodology, Visualization. CGF—Investigation, Visualization. TJH—Funding acquisition, Conceptualization, Methodology, Supervision, Writing—Review & Editing.**FUNDING**

Office of Science (DE-SC0021700), Paul R. Carriere, National Science Foundation (ECCS-2025064)

CONFLICT OF INTEREST

The authors declare that they have no conflict of interest.

OPEN ACCESS

REFERENCES

1. C. Agte and J. Vacek, *Tungsten and Molybdenum* (National Aeronautics and Space Administration Office of Scientific and Technical Information, Washington, 1963).
2. R.A. Pitts, S. Carpentier, F. Escourbiac, T. Hirai, V. Komarov, S. Lisgo, A.S. Kukushkin, A. Loarte, M. Merola, A. Sashala Naik, R. Mitteau, M. Sugihara, B. Bazylev, and P.C. Stangeby, *J. Nucl. Mater.* 438, S48 (2013).
3. R.E. Nygren, D.L. Youchison, B.D. Wirth, and L.L. Snead, *Fusion Eng. Des.* 109–111, 192 (2016).
4. Y. Katoh, L.L. Snead, L.M. Garrison, X. Hu, T. Koyanagi, C.M. Parish, P.D. Edmondson, M. Fukuda, T. Hwang, T. Tanaka, and A. Hasegawa, *J. Nucl. Mater.* 520, 193 (2019).
5. E. Lassner and W.-D. Schubert, *Tungsten: Properties, Chemistry, Technology of the Element, Alloys, and Chemical Compounds* (Springer, Boston, MA, 1999).
6. J. Choi, H.-M. Sung, K.-B. Roh, S.-H. Hong, G.-H. Kim, and H.N. Han, *Int. J. Refract. Met. Hard Mater.* 69, 164 (2017).
7. S. Deng, T. Yuan, R. Li, F. Zeng, G. Liu, and X. Zhou, *Powder Technol.* 310, 264 (2017).
8. T. DebRoy, H.L. Wei, J.S. Zuback, T. Mukherjee, J.W. Elmer, J.O. Milewski, A.M. Beese, A. Wilson-Heid, A. De, and W. Zhang, *Prog. Mater. Sci.* 92, 112 (2018).
9. A.V. Müller, D. Dorow-Gerspach, M. Balden, M. Binder, B. Buschmann, B. Curzadd, T. Loewenhoff, R. Neu, G. Schlick, and J.H. You, *J. Nucl. Mater.* 566, 153760 (2022).
10. A. Talignani, R. Seede, A. Whitt, S. Zheng, J. Ye, I. Karaman, M.M. Kirka, Y. Katoh, and Y.M. Wang, *Addit. Manuf.* 58, 103009 (2022).
11. K.-L. Li, J.-H. Chen, C.-C. Zhao, Z.-J. Shen, and W. Liu, *Tungsten* 3, 218 (2021).
12. M. Minissale, C. Pardanaud, R. Bisson, and L. Gallais, *J. Phys. D: Appl. Phys.* 50, 455601 (2017).
13. J. Zhang, D. Gu, Y. Yang, H. Zhang, H. Chen, D. Dai, and K. Lin, *Engineering* 5, 736 (2019).
14. D. Wang, C. Yu, X. Zhou, J. Ma, W. Liu, and Z. Shen, *Appl. Sci.* 7, 430 (2017).
15. J. Chen, K. Li, Y. Wang, L. Xing, C. Yu, H. Liu, J. Ma, W. Liu, and Z. Shen, *Int. J. Refract. Met. Hard Mater.* 87, 105135 (2020).
16. A.T. Sidambe and P. Fox, Interaction of pure tungsten powder with processing conditions in selective laser melting. in *Advances in Powder Metallurgy and Particulate Materials 2017-Proceedings of the 2017 International Conference on Powder Metallurgy and Particulate Materials* (2017), p. 701–711.
17. A.T. Sidambe, D.S. Judson, S.J. Colosimo, and P. Fox, *Int. J. Refract. Met. Hard Mater.* 84, 104998 (2019).
18. A.T. Sidambe, Y. Tian, P.B. Prangnell, and P. Fox, *Int. J. Refract. Met. Hard Mater.* 78, 254 (2019).
19. A. Sidambe and P. Fox, Analysis of melt pool during the laser powder bed fusion of Tungsten. in *RAPDASA 2019 Conference and Exhibition*, Bloemfontein, South Africa (2020).
20. A. Iveković, N. Omidvari, B. Vrancken, K. Lietaert, L. Thijs, K. Vanmeensel, J. Vleugels, and J.-P. Kruth, *Int. J. Refract. Met. Hard Mater.* 72, 27 (2018).
21. M. Guo, D. Gu, L. Xi, L. Du, H. Zhang, and J. Zhang, *Int. J. Refract. Met. Hard Mater.* 79, 37 (2019).
22. C. Tan, K. Zhou, W. Ma, B. Attard, P. Zhang, and T. Kuang, *Sci. Technol. Adv. Mater.* 19, 370 (2018).
23. M.S. Seyam, P. Koshy, and M.A. Elbestawi, *Metals* 12, 274 (2022).

24. A.V. Müller, G. Schlick, R. Neu, C. Anstätt, T. Klimkait, J. Lee, B. Pascher, M. Schmitt, and C. Seidel, *Nucl. Mater. Energy* 19, 184 (2019).
25. Q. Shi, W. Du, F. Qin, C. Tan, K. Khanlari, H. Xie, X. Liu, and A. Wu, *J. Mater. Eng. Perform.* https://doi.org/10.1007/s11665-023-07891-9 (2023).
26. J. Dong, S. Liu, H. Chen, D. Li, T. Zhang, C. Chen, and K. Zhou, *Mater. Sci. Technol.* 36, 1988 (2020).
27. U. Scipioni Bertoli, A.J. Wolfer, M.J. Matthews, J.-P.R. Delplanque, and J.M. Schoenung, *Mater. Des.* 113, 331 (2017).
28. Z. Xiong, P. Zhang, C. Tan, D. Dong, W. Ma, and K. Yu, *Adv. Eng. Mater.* 22, 1901352 (2020).
29. C. Ren, Z.Z. Fang, M. Koopman, B. Butler, J. Paramore, and S. Middlemas, *Int. J. Refract. Met. Hard Mater.* 75, 170 (2018).
30. G.L. Krasko, *Int. J. Refract. Met. Hard Mater.* 12, 251 (1993).
31. J. Braun, L. Kaserer, J. Stajkovic, K.-H. Leitz, B. Tabernig, P. Singer, P. Leibenguth, C. Gspan, H. Kestler, and G. Leichtfried, *Int. J. Refract. Met. Hard Mater.* 84, 104999 (2019).
32. B. Gludovatz, S. Wurster, T. Weingärtner, A. Hoffmann, and R. Pippan, *Philos. Mag.* 91, 3006 (2011).
33. D.-Z. Wang, K.-L. Li, C.-F. Yu, J. Ma, W. Liu, and Z.-J. Shen, *Acta Metall. Sin. (Engl. Lett.)* 32, 127 (2019).
34. X. Zhou, X. Liu, D. Zhang, Z. Shen, and W. Liu, *J. Mater. Process. Technol.* 222, 33 (2015).
35. B. Vrancken, R.K. Ganeriwala, and M.J. Matthews, *Acta Mater.* 194, 464 (2020).
36. B. Vrancken, W.E. King, and M.J. Matthews, *Procedia CIRP* 74, 107 (2018).
37. S. Wen, C. Wang, Y. Zhou, L. Duan, Q. Wei, S. Yang, and Y. Shi, *Opt. Laser Technol.* 116, 128 (2019).
38. E.A.I. Ellis, M.A. Sprayberry, C. Ledford, J.P. Hankwitz, M.M. Kirka, C.D. Rock, T.J. Horn, Y. Katoh, and R.R. Dehoff, *J. Nucl. Mater.* 555, 153041 (2021).
39. C. Ledford, P. Fernandez-Zelaia, T. Graening, Q. Campbell, J.O. Rojas, A.M. Rossy, Y. Kato, and M.M. Kirka, *Int. J. Refract. Met. Hard Mater.* 113, 106148 https://doi.org/10.1016/j.ijrmhm.2023.106148 (2023).
40. S.S. Babu, L. Love, R. Dehoff, W. Peter, T.R. Watkins, and S. Pannala, *MRS Bull.* 40, 1154 (2015).
41. C. Körner, *Int. Mater. Rev.* 61, 361 (2016).
42. C. Li, M.F. Gouge, E.R. Denlinger, J.E. Irwin, and P. Michaleris, *Addit. Manuf.* 26, 258 (2019).
43. G. Yang, P. Yang, K. Yang, N. Liu, L. Jia, J. Wang, and H. Tang, *Int. J. Refract. Met. Hard Mater.* 84, 105040 (2019).
44. J. Wright, *Additive Manufacturing of Tungsten via Selective Laser Melting and Electron Beam Melting* (University of Sheffield, Sheffield, 2019).
45. D. Dorow-Gerspach, A. Kirchner, T. Loewenhoff, G. Pintsuk, T. Weißgärber, and M. Wirtz, *Nucl. Mater. Energy* 28, 101046 (2021).
46. X. Ren, H. Peng, J. Li, H. Liu, L. Huang, and X. Yi, *Materials* 15, 1172 (2022).
47. U. Ackelid, *Method and Apparatus for Increasing the Resolution in Additively Manufactured Three-dimensional Articles* (USPTO Patent Center, Alexandria, 2015).
48. C. Ledford, M. Tung, C. Rock, and T. Horn, *Addit. Manuf.* 34, 101365 (2020).
49. K. Li, D. Wang, L. Xing, Y. Wang, C. Yu, J. Chen, T. Zhang, J. Ma, W. Liu, and Z. Shen, *Int. J. Refract. Met. Hard Mater.* 79, 158 (2019).
50. J. Xue, Z. Feng, J. Tang, C. Tang, and Z. Zhao, *J. Alloys Compd.* 874, 159879 (2021).
51. J. Habainy, S. Iyengar, K.B. Surreddi, Y. Lee, and Y. Dai, *J. Nucl. Mater.* 506, 26 (2018).
52. P. Morcos, A. Elwany, I. Karaman, and R. Arróyave, *J. Mater. Sci.* 57, 9769 (2022).
53. I. Gibson, D. Rosen, B. Stucker, and M. Khorasani, *Additive Manufacturing Technologies* (Springer, Cham, 2021).
54. J.D. Hunt, *Mater. Sci. Eng.* 65, 75 (1984).
55. S.C. Flood and J.D. Hunt, *J. Cryst. Growth* 82, 552 (1987).
56. S.C. Flood and J.D. Hunt, *J. Cryst. Growth* 82, 543 (1987).
57. S. Kou, *Welding Metallurgy*, 3rd edn. (Wiley, Hoboken, 2021).
58. W. Kurz, B. Giovanola, and R. Trivedi, *Acta Metall.* 34, 823 (1986).
59. P.A. Kobryn and S.L. Semiatin, *J. Mater. Process. Technol.* 135, 330 (2003).
60. J.J. Blecher, T.A. Palmer, and T. DebRoy, *Metall. Mater. Trans. A* 45, 2142 (2014).
61. M.M. Kirka, Y. Lee, D.A. Greeley, A. Okello, M.J. Goin, M.T. Pearce, and R.R. Dehoff, *JOM* 69, 523 (2017).
62. R.R. Dehoff, M.M. Kirka, W.J. Sames, H. Bilheux, A.S. Tremsin, L.E. Lowe, and S.S. Babu, *Mater. Sci. Technol.* 31, 931 (2015).
63. N. Raghavan, R. Dehoff, S. Pannala, S. Simunovic, M. Kirka, J. Turner, N. Carlson, and S.S. Babu, *Acta Mater.* 112, 303 (2016).
64. P. Frigola, O.A. Harrysson, T.J. Horn, H.A. West, R.L. Aman, J.M. Rigsbee, D.A. Ramirez, L.E. Murr, F. Medina, R.B. Wicker, and E. Rodriguez, *Adv. Mater. Process.* 172, 20 (2014).
65. R. Guschlbauer, S. Momeni, F. Osmanlic, and C. Körner, *Mater. Charact.* 143, 163 (2018).
66. P. Tarafder, *Characterization of Mechanical Properties and Evaluation of Methods for Grain Control of Copper Fabricated Using EB-PBF Process* (North Carolina State University, Raleigh, 2021).
67. M.R. Staker and D.L. Holt, *Acta Metall.* 20, 569 (1972).
68. Y. Xia, P. Hu, K.-S. Wang, S.-L. Li, H.-R. Xing, T. Chang, P.-F. Feng, and L.-P. Li, *Mater. Charact.* 159, 110010 (2020).
69. Z.S. Courtright and K.M. Benensky, *NASA/TM* 1486, 220135 (2019).
70. R. Cortenraad, S.N. Ermolov, V.N. Semenov, A.W. Denier van der Gon, V.G. Glebovsky, S.I. Bozhko, and H.H. Brongersma, *J. Cryst. Growth* 222, 154 (2001).
71. P. Fernandez-Zelaia, C. Ledford, E.A.I. Ellis, Q. Campbell, A.M. Rossy, D.N. Leonard, and M.M. Kirka, *Mater. Des.* 207, 109809 (2021).
72. W.A. Witzen, A.T. Polonsky, P.F. Rottmann, K.M. Pusch, M.P. Echlin, T.M. Pollock, and I.J. Beyerlein, *J. Mater. Sci.* 57, 9885 (2022).
73. C. Wang, D. Chen, Y. Zhou, Z. Xie, Q. Fang, S. Wen, and C. Yan, *Chin. J. Mech. Eng.* 35, 48 (2022).